Large Silicon Abundance in Photodissociation Regions[1]

Yoko Okada and Takashi Onaka

Department of Astronomy, Graduate School of Science, University of Tokyo, Bunkyo-ku, Tokyo, 113-0033, Japan

okada@astron.s.u-tokyo.ac.jp; onaka@astron.s.u-tokyo.ac.jp

Takao Nakagawa

Department of Infrared Astrophysics, Institute of Space and Astronautical Science (ISAS), Japan Aerospace Exploration Agency (JAXA), Kanagawa, 229-8510, Japan

Hiroshi Shibai

Graduate School of Science, Nagoya University, Nagoya, 464-8602, Japan

Daigo Tomono

Subaru Telescope, National Astronomical Observatory of Japan, Hilo, Hawaii 96720, U.S.A.

and

Yukari Y. Yui

Earth Observation Research and Application Center, Office of Space Applications, Japan Aerospace Exploration Agency (JAXA), Tokyo, 104-6023, Japan

ABSTRACT

We have made one-dimensional raster-scan observations of the ρ Oph and σ Sco star-forming regions with two spectrometers (SWS and LWS) on board the *ISO*. In the ρ Oph region, [Si II] $35\,\mu$m, [O I] $63\,\mu$m, $146\,\mu$m, [C II] $158\,\mu$m, and the H_2 pure rotational transition lines S(0) to S(3) are detected, and the PDR properties are derived as the radiation field scaled by the solar neighborhood value $G_0 \sim 30$–500, the gas density $n \sim 250$–2500 cm^{-3}, and the surface temperature $T \sim 100$–400 K. The ratio of [Si II] $35\,\mu$m to [O I] $146\,\mu$m indicates that silicon of 10–20% of the solar abundance must be in the gaseous form in the photodissociation region (PDR), suggesting that efficient dust destruction is undergoing even in the PDR and that part of silicon atoms may be contained in volatile forms in dust grains. The [O I] $63\,\mu$m and [C II] $158\,\mu$m emissions are too

weak relative to [O I] 146 μm to be accounted for by standard PDR models. We propose a simple model, in which overlapping PDR clouds along the line of sight absorb the [O I] 63 μm and [C II] 158 μm emissions, and show that the proposed model reproduces the observed line intensities fairly well. In the σ Sco region, we have detected 3 fine-structure lines, [O I] 63 μm, [N II] 122 μm, and [C II] 158 μm, and derived that 30–80% of the [C II] emission comes from the ionized gas. The upper limit of the [Si II] 35 μm is compatible with the solar abundance relative to nitrogen and no useful constraint on the gaseous Si is obtained for the σ Sco region.

Subject headings: infrared: ISM: lines and band – PDR – ISM: individual objects: ρ Oph cloud

1. Introduction

Silicon and carbon are major constituents of interstellar grains (Mathis 1990). The gas phase Si abundance is about 5% of solar in cool clouds (Savage & Sembach 1996) and the depleted atoms are thought to reside in interstellar grains. According to the observations of UV absorption lines, Si shows a systematic trend of depletion with the density of the diffuse cloud as well as Mg and Fe (Jenkins et al. 1986; Harris et al. 1984), whereas the depletion of Fe is suggested not to continue to increase with either density or extinction for $\langle n_{\rm H} \rangle \gtrsim 1$ cm^{-3} (Snow et al. 2002). Sofia et al. (1994) suggested that Fe has the greatest fraction of its atoms incorporated into dust followed by Mg and Si, and suggested oxides and/or metallic Fe as the grain core population. Fitzpatrick (1996) showed that the gas-phase abundance of Si and Fe is well correlated with each other to some extent, but the degree of returning to the gas phase is different between the two: it is easier for Si to return to the gas than for Fe. This suggests that at least part of Si and Fe atoms constitute independent grain populations. Jones (2000) examined the relation among the depletion of Si, Mg, and Fe, suggesting that Si in dust is preferentially eroded with respect to Mg and that both of these elements are preferentially eroded with respect to Fe. This cannot completely be explained by mechanical sputtering process, indicating some chemically selective processes involved or the presence of Si in phases other than refractory silicates. Frisch & Slavin (2003) showed that the gas-to-dust ratio in the local ISM is well correlated with the fraction of the dust mass carried by

Fe. This indicates that Fe forms a robust core that is not destroyed during grain processing in the ISM. Cartledge et al. (2004) showed that the dust phase abundance of O derived with the "missing mass" method is consistent with the grain model in which silicates are primarily Mg based and most or all of Fe is in metal or oxides. On the other hand, C, N, and O abundance is relatively constant against the gas density (Sofia et al. 1997; Cardelli et al. 1996; André et al. 2003; Jensen et al. 2005), although the dependence on the density for oxygen is also reported (Cartledge et al. 2001, 2004).

Depletion in active star-forming regions, where the density is much higher than diffuse clouds, has been studied by infrared line emissions. Intense [Si II] $35\,\mu$m emission has been reported in a shocked region in Orion (Haas et al. 1991), the Galactic center region (Stolovy et al. 1995), the Carina region (Mizutani et al. 2004), and the starburst galaxy NGC 253 (Carral et al. 1994). Not only in ionized regions but also in photodissociation regions (PDRs) large gas phase abundances of Si have been reported: 30% of the solar abundance in Sharpless 171 (S171) (Okada et al. 2003, hereafter OOSD03); 50% in G333.6-0.2 H II region (Colgan et al. 1993); 20–30% in the reflection nebula NGC 7023 (Fuente et al. 2000); 10% in OMC-1 (Rosenthal et al. 2000). Young Owl et al. (2002) observed nine reflection nebulae and detected [Si II] $35\,\mu$m in two regions with the density range of 0.9–2×10^4 cm^{-3} and indicated that the intensities of [Si II] $35\,\mu$m in those regions agree with the PDR model. The conversion of the [Si II] $35\,\mu$m intensity to the Si abundance depends on the physical properties, especially the gas density, and thus we need to derive those properties from other line emissions.

In this paper, we report detection of intense [Si II] $35\,\mu$m emission in the ρ Oph reflection nebula based on observations with the Short-Wavelength Spectrometer (SWS; de Graauw et al. 1996) and the Long-Wavelength Spectrometer (LWS; Clegg et al. 1996) on board the *Infrared Space Observatory* (*ISO*; Kessler et al. 1996). We discuss the constraint on the Si abundance in the PDR gas, as well as the physical properties of the PDR. Preliminary results have been reported in Tomono et al. (1997). The ρ Oph region is a giant group of molecular clouds which is associated with the Sco OB2 association (Loren 1989). The dense region in the eastern part is known as the ρ Oph main cloud, containing three B-type stars (Yui et al. 1993). The ρ Oph region is well studied by far-infrared forbidden lines (Liseau et al. 1999; Yui et al. 1993), H$_2$ (Habart et al. 2003), CO (Nozawa et al. 1991; Loren 1989), and [C I] emission (Kamegai et al. 2003). Liseau et al. (1999) made mapping observations of a wide area of the ρ Oph main cloud with the LWS on board the *ISO* and derived physical properties of the PDR. They suggested that the [O I] $63\,\mu$m to $146\,\mu$m ratio is too small (< 5) to be accounted for by PDR models. Habart et al. (2003) made high spatial-resolution observations of H$_2$ pure rotational and ro-vibrational transitions in the northern-western part with the SWS. They derived that the ortho-to-para (OTP) ratio is

close to unity and suggested that the H_2 formation rate must be high in the warm gas. Here we report one-dimensional raster-scan observations with the SWS and LWS, which give us the spatial distribution of [Si II] $35\,\mu$m emission and the correlation with other line emissions from the PDR, and provide a constraint on the Si abundance in the PDR gas.

In addition, we observed a region around σ Sco, a B1 type star located south-west of the ρ Oph region in order to examine PDR properties and the Si abundance in the same association as ρ Oph. Baart et al. (1980) suggested the presence of a spherical H II region around σ Sco from the radio continuum emission. Yui et al. (1993) detected extended [C II] emission with a small peak near σ Sco. de Geus et al. (1990) did not detect the CO line emission around σ Sco, which indicates that the interstellar gas around σ Sco is almost completely photodissociated.

2. Observations and data reduction

The observations were carried out at 32 positions in the ρ Oph cloud (Fig. 1 and Tables 1 and 2), each of which was separated by $3'$, or 0.12 pc at the distance of the ρ Oph cloud of 136 pc (Perryman et al. 1997). The position number (p#) is designated to increase from west to east (toward the molecular cloud; see Fig. 1). The exciting source HD 147889 is located between p13 and p14. A peak of ^{13}CO is located near p19. For the σ Sco region, one-dimensional raster-scan observations were carried out through σ Sco toward the north-west direction, where the [C II] $158\,\mu$m and the IRAS $100\,\mu$m continuum emissions show an extended structure (Yui et al. 1993). The observations were carried out at 15 positions (Table 3), each of which was separated by $3'$. The position number (p#) is designated from north-west to south-east. The exciting source σ Sco is located between p13 and p14 (see Fig. 1).

For both regions, the line profile mode AOT SWS02 was used in the SWS observations to observe [Si II] $35\,\mu$m and the H_2 pure rotational transition S(3) at $9.66\,\mu$m in the cycle 1 observation. The aperture size was $14'' \times 20''$ and $20'' \times 33''$, the spectral resolution $\lambda/\Delta\lambda$ was 1500 and 2000, and the flux calibration accuracy for point-like sources was 7% and 22% (Leech et al. 2003) for H_2 S(3) and [Si II] $35\,\mu$m emissions, respectively. Further observations were made from p13 to p20 for other H_2 pure rotational and ro-vibrational transitions in the ρ Oph region in the cycle 2 (Table 2). The aperture size for each transition line observation is not the same (Table 2). The Off-Line Processing (OLP) version 10.1 data obtained from the ISO Archival Data Center were used for the present study. At each raster position one up-and-down grating scan was carried out. The spectra were further processed by using

the ISO Spectral Analysis Package (ISAP[2]) in the same manner as for S171 (OOSD03). The conversion factors for extended sources are taken from Leech et al. (2003), which are estimated to be accurate within 10%. The line intensities were derived by Gaussian fits.

The same positions were observed with the LWS full grating scan mode AOT LWS01 to cover the wavelength range from 43 to 197 μm with $\lambda/\Delta\lambda \sim 100$–300 (Gry et al. 2003). Four grating scans were carried out for each raster position with the spectral sampling of half the resolution element. The total integration time at a grating position was 2 sec. The LWS beam size was 66″–86″, depending on the wavelength (Gry et al. 2003). The OLP 10.1 data were used in the present study. We used the ISAP for further data processing and derived the line intensities by Gaussian fits. The absolute flux calibration uncertainty is reported to be 10–20% for point sources and 50% for extended sources (Gry et al. 2003).

3. Results and Discussions

In the ρ Oph region, we detected 2 lines, H_2 S(3) 9.66 μm and [Si II] 35 μm in the SWS spectra and 3 forbidden lines, [O I] 63 μm, [O I] 146 μm, and [C II] 158 μm in the LWS spectra for the cycle 1 observations. In the cycle 2 we detected three pure rotational lines of H_2, S(2) 12.3 μm, S(1) 17.0 μm, and S(0) 28.2 μm. The results are summarized in Tables 1 and 2. The detected ionic lines arise only from elements with ionization potential less than that of hydrogen (C and Si), i.e., no higher ionization lines, such as [N II] 122 μm nor [O III] 88 μm, have been detected, being consistent with the absence of a radio continuum emission peak around HD 147889 (Baart et al. 1980). The [O I] 146 μm line was observed by two adjacent detectors, LW3 and LW4. The line intensities derived from different detectors are in agreement with each other within the estimated uncertainties. We use the weighted mean of the intensities from the two detectors in the following analysis. In the case that the line was detected only by one detector with the other being an upper limit, we adopted the intensity of the detected channel.

The results of the σ Sco region are summarized in Table 3. [Si II] 35 μm and H_2 9.66 μm have not been detected at any positions in the SWS spectra. In the LWS spectra we detected 3 forbidden lines, [O I] 63 μm, [N II] 122 μm, and [C II] 158 μm. The [N II] 122 μm emission traces the low density ionized gas and the detection of this line is consistent with the presence of the radio continuum emission peak (Baart et al. 1980). On the other hand, the lack of emission lines from highly ionized ions such as [O III] and [N III] is

---

consistent with the late spectral type (B1) of the exciting star.

The errors in the line intensities include both the fitting errors and the statistical errors of the baseline. Uncertainties in the absolute flux are not included in the errors in Tables 1–3. For the line emission less than 3 times the uncertainty ($< 3\sigma$) we regard it as non-detection and give 3σ as the upper limit. For each region, the lines not listed in Tables 1–3 are not detected at all the observed positions and only upper limits are derived as: [O III] $52\,\mu$m $<$ 2.7×10^{-7}, [N III] $57\,\mu$m $<$ 2.0×10^{-7}, [O III] $88\,\mu$m $<$ 6.9×10^{-8} and [N II] $122\,\mu$m $<$ $3.6 \times 10^{-8}\,\mathrm{W\,m^{-2}\,sr^{-1}}$ for the ρ Oph region, H_2 $9.66\,\mu$m $<$ 3.6×10^{-8}, [Si II] $35\,\mu$m $<$ 6.4×10^{-8}, [O III] $52\,\mu$m $<$ 5.3×10^{-8}, [N III] $57\,\mu$m $<$ 4.9×10^{-8}, [O III] $88\,\mu$m $<$ 3.2×10^{-8}, and [O I] $146\,\mu$m $<$ $3.7 \times 10^{-9}\,\mathrm{W\,m^{-2}\,sr^{-1}}$ for the σ Sco region.

Figures 2 and 3 show the spatial distributions of the line intensities for the ρ Oph and the σ Sco regions. For the ρ Oph region, the line emissions other than [C II] $158\,\mu$m are detected only at p13–p20 and p23, near the surface regions of the molecular clouds. The [C II] $158\,\mu$m emission is detected at all the observed positions and shows a peak at p15. This is consistent with the result of Yui et al. (1993), who reported an extended distribution of the [C II] emission.

3.1. PDR properties

We estimate the properties of the PDR from the observed lines and continuum emission using the PDR model by Kaufman et al. (1999). The major model parameters are the gas density, n, and the UV radiation field strength, G_0, in units of the solar neighborhood value (Habing 1968, $1.6 \times 10^{-6}\,\mathrm{W\,m^{-2}}$). The model gives integrated line intensities seen in the face-on view. In the following, we discuss only the results of the positions where all the [O I] $63\,\mu$m, $146\,\mu$m, and [C II] $158\,\mu$m emissions are detected (p14–p20). Although any appreciable amount of the ionized gas has not been detected in the ρ Oph region, part of [C II] $158\,\mu$m may come from the undetected ionized gas. From 2.3GHz radio continuum observations (Emission measure $= 176\,\mathrm{pc\,cm^{-6}}$; Baart et al. 1980) we estimate the contribution of the [C II] $158\,\mu$m emission from the ionized gas to be less than 6% assuming the low-density limit condition and the interstellar abundance (Savage & Sembach 1996). This fraction is smaller than the uncertainty in the observed intensity. Possible contribution from the ionized gas thus will not affect the following discussion on the PDR properties within the observational uncertainties. Comparison between the observation and the PDR model can be made less ambiguously for the ρ Oph region than for H II regions, such as S171 (OOSD03).

The ratio of the observed [O I] $63\,\mu$m/[O I] $146\,\mu$m is too small (3–7) compared to PDR models of any parameter range, and no PDR models can account for the observed line intensities of [O I] $63\,\mu$m, $146\,\mu$m, and [C II] $158\,\mu$m consistently. The small ratio of [O I] $63\,\mu$m/[O I] $146\,\mu$m in the ρ Oph region has been reported by Liseau et al. (1999) and is attributed to the optically thick emission of [O I] $63\,\mu$m (Caux et al. 1999). To derive the physical properties of the PDR and explain quantitatively the discrepancy between the observed line intensities and the prediction from the PDR model by Kaufman et al. (1999), we adopt a simple model that was applied for S171 (OOSD03). [O I] $63\,\mu$m is optically thick, [C II] $158\,\mu$m is marginally thick ($\tau \sim 1$), and [O I] $146\,\mu$m and the FIR continuum emission are optically thin in a PDR (Kaufman et al. 1999). OOSD03 suggest that overlapping PDR clouds along the line of sight attenuate the former two line emissions, while the intensities of the latter two will be a simple summation of those from each PDR cloud. Therefore, we use the [O I] $146\,\mu$m to the total far-infrared intensity (FIR) ratio and G_0 as input parameters to estimate the density and the surface temperature using the PDR model (Figs. 4a–c). We fit the continuum emission of the LWS spectra with a graybody radiation of the λ^{-1} emissivity and estimate G_0 by assuming $\langle\tau_{\mathrm{abs}}\rangle/\tau_{100} = 700$ and $f = 0.5$, where $\langle\tau_{\mathrm{abs}}\rangle$ is the weighted mean of the absorption optical depth over the mean intensity from the heating source, τ_{100} is the optical depth at $100\,\mu$m, and f is the ratio of the energy between 6 eV and 13.6 eV to the total luminosity for the spectrum of HD 147889 of a blackbody of $T_{\mathrm{eff}} = 20300$ K (see OOSD03 for details). Models with these parameters predict the [O I] $63\,\mu$m and [C II] $158\,\mu$m emissions stronger than observed. It can be explained by taking into account of the overlapping factor Z defined as

$$Z = \frac{FIR(\mathrm{obs})}{FIR(\mathrm{model})}, \tag{1}$$

where $FIR(\mathrm{model}) = 1.6 \times 10^{-6}\, G_0/4\pi f\ \mathrm{W\,m^{-2}\,sr^{-1}}$ with the assumption that all the incident radiation is absorbed and converted into the FIR emission. Z is equal to the beam filling factor for $Z < 1$, whereas it indicates the degree of overlapping of clouds for $Z > 1$ since the FIR emission is optically thin. Figure 4d shows the estimated Z with the errors including the absolute flux uncertainty of the LWS. At the positions of p14–p20, Z is larger than unity, suggesting that the effect of overlapping clouds is significant. We assume that the size of a cloud is smaller than the beam ($\lesssim 0.06$ pc), and the column density for [O I] $63\,\mu$m in a cloud is sufficiently large ($N_{\mathrm{H+H_2}} \gtrsim 5 \times 10^{21}$ cm^{-2}). To examine the effect of the overlapping on the observed intensity we simply assume that N identical clouds overlap on the line of sight and attenuate the line emissions. Then the observed [O I] $63\,\mu$m and [C II] $158\,\mu$m should be attenuated by a factor of

$$\frac{\sum_{j=0}^{N-1} e^{-j\tau}}{N} = \frac{1 - e^{-N\tau}}{N(1 - e^{-\tau})}, \tag{2}$$

where the number of clouds N can be substituted by Z (OOSD03). We assume $\tau = \infty$ for [O I] $63\,\mu$m and $\tau = 1$ for [C II] $158\,\mu$m. The corrected [O I] $63\,\mu$m and [C II] $158\,\mu$m intensities together with the observed [O I] $146\,\mu$m and the FIR emissions can be accounted for by the PDR model of G_0 and n of Figs 4a and b within 1σ except for p14 and p15, where the model prediction of the [O I] $63\,\mu$m is still slightly larger than the observed intensities (Figs. 4e and f). In Figs. 4e and f, the errors in the model prediction include the uncertainty in the derived parameters (G_0 and n), whereas those in the observed intensities include the uncertainties in the original intensity (Table 1) and those in Z (Fig. 4d). The derived distributions of G_0, n and the surface temperature are compatible with the CO observations and the location of the exciting source. In the present estimate, we assume that the cloud density is the same among PDRs along the line of sight to simplify the calculation and the derived density represents a mean value of the true distribution. The agreement of the model prediction with the corrected line intensities at 5 positions supports interpretation by overlapping PDR clouds for the line intensities in a semi-quantitative way.

For all the 15 observed positions in the σ Sco region we find $Z < 1$, which indicates that the [O I] $63\,\mu$m emission is unlikely to be attenuated by overlapping PDR clouds. Therefore, we use the [O I] $63\,\mu$m emission instead of the [O I] $146\,\mu$m emission to derive the PDR properties (Figs. 5a–c). σ Sco is associated with a H II region and the [C II] $158\,\mu$m emission originates both from the ionized and the PDR gas. The [C II] $158\,\mu$m intensity predicted by the PDR model is smaller than those observed (Fig. 5d). The excess intensity is attributed to the emission from the ionized gas. The contribution from the ionized gas is 30–80% at three positions closest to the excitation star (p5, p6, and p7). Yui et al. (1993) suggested that the [C II] $158\,\mu$m emission comes from the neutral gas adjacent to the H II region based on the poor correlation between the radio continuum and the [C II] $158\,\mu$m emission. The present results indicate that a non-negligible fraction of the [C II] $158\,\mu$m emission comes from the ionized gas in the σ Sco region.

3.2. Silicon abundance in the PDR

In the ρ Oph region, we have detected strong [Si II] $35\,\mu$m emission. With the gas density $\sim 10^3$ cm^{-3} and $G_0 \sim 10^3$, the PDR model (Hollenbach et al. 1991) predicts the [Si II] $35\,\mu$m to the [O I] $146\,\mu$m intensity ratio to be ~ 0.4, while the observation shows the ratio of ~ 2–4 (Fig. 6). The abundance of Si is assumed to be 2.3% of the solar abundance in the model. If we attribute the difference to the abundance or the depletion degree of Si, it suggests that 10–20% of the solar abundance of Si must reside in the gas phase in the PDR of ρ Oph. The optical depth of [Si II] $35\,\mu$m in a typical PDR is about 0.1 and

thus the overlapping effect is negligible. The [Si II] $35\,\mu$m and [O I] $146\,\mu$m transitions have similar excitation energies (413 K and 327 K, respectively) and both transitions as well as [O I] $63\,\mu$m have critical densities higher than 10^5 cm^{-3} with the collision partner of atomic hydrogen. The calculation for isothermal cloud with a uniform density with the optically thin condition shows that the [Si II] $35\,\mu$m to the [O I] $146\,\mu$m ratio is not dependent on the gas density for $n \lesssim 10^4$ cm^{-3} and not sensitive to the gas temperature for $T \gtrsim 300$ K. In fact PDR model calculations suggest that the ratio changes only by 10% for $n < 10^4$ cm^{-3} and $10^2 \lesssim G_0 \lesssim 10^3$ (Wolfire et al. 1990). Meixner & Tielens (1993) showed that clumpy PDRs can increase the [Si II] $35\,\mu$m to [O I] $146\,\mu$m intensity ratio by a factor of 1.5. Clumpiness alone can not fully account for the observed large ratio. Liseau et al. (1999) showed that the density of the PDR in the ρ Oph main cloud is $(1\text{–}3)\times 10^4$ cm^{-3}, which is by one order of magnitude larger than the present result. The discrepancy comes from the difference of the employed PDR models: the model by Kaufman et al. (1999) takes account of the heating by PAHs that produces strong [O I] emissions at low densities. The [Si II] $35\,\mu$m to the [O I] $146\,\mu$m intensity ratio is not sensitive to the density as mentioned above, and thus the large ratio must be attributed to the large Si abundance irrespective of the assumed density. As the [C II] $158\,\mu$m emission, the [Si II] $35\,\mu$m emission can originate from the ionized gas. We estimate from the radio continuum observation (Baart et al. 1980) that only 30% of the observed [Si II] $35\,\mu$m emission can be attributed to the ionized gas even if the gaseous Si abundance is solar. Therefore most [Si II] $35\,\mu$m emission should come from the PDR and the possible contribution from the ionized gas will not affect the above discussion on the large gas phase abundance of Si in the PDR.

The column density of Si included in dust grains can be estimated from the dust model and τ_{100}, which is derived from the graybody fit of the continuum spectra. We use the dust model by Draine & Lee (1984) with the assumptions of the density of dust grains of $3.3\,\mathrm{g\,cm}^{-3}$ and the mean molecular weight of 100–200 for olivine and pyroxene. On the other hand, we can estimate the column density of Si$^+$ from the [Si II] $35\,\mu$m intensity, the gas density, and the gas temperature. We use the density and the surface temperature derived from the PDR model in §3.1 in the following discussion. For a given intensity, the column density decreases with the temperature and thus a highest likely temperature gives a lower limit of the column density. Figure 7 plots the column density of Si in gas against that in dust. It indicates that the relative fraction of Si in the gas and dust phases is in agreement with the result from the [Si II] $35\,\mu$m/[O I] $146\,\mu$m ratio. Note that this estimate is independent of the assumed solar abundance. If the density is higher by one order of magnitude as suggested by Liseau et al. (1999), we obtain a lower column density of Si in the gas phase by one order of magnitude. Then [Si II] $35\,\mu$m/[O I] $146\,\mu$m is estimated to be lower than observed. The gas phase abundance of Si estimated from [Si II] $35\,\mu$m and τ_{100} supports the present estimate of

the gas density ($\sim 10^3$ cm^{-3}), though we cannot exclude the higher density because of large uncertainties.

The temperature of H$_2$ emitting gas can be estimated from the ratio of the H$_2$ line emissions. Assuming the Boltzmann distribution at low-J transitions and the homogeneous distribution of the emissions in the aperture we derive the temperature of ortho H$_2$ to be 298$\pm$12 K, 315$\pm$20 K, 310$\pm$9 K, and 307$\pm$8 K at p15–p18 in the ρ Oph region, respectively, from the line intensities of 9.66 μm and 17.0 μm. Although the aperture size for each line is not the same (Table 2), similar temperatures derived at 4 positions suggest that the differences in the aperture size do not significantly affect the estimates. At p18, we also detect two lines from para H$_2$ at 12.3 μm and 28.2 μm, and derive the temperature as 260$\pm$21 K, which gives a similar temperature as that from ortho H$_2$ lines. The temperature of the H$_2$ emitting gas is in a range similar to the surface temperature. If we use the temperature of H$_2$ emission to estimate the column density of gaseous Si$^+$, the conclusion remains unchanged.

According to theoretical investigations, dust grains in the interstellar space are destroyed in a time scale of (2–4)$\times 10^8$ yr by supernova shock waves (Jones et al. 1994, 1996). However, the gas densities of the PDR are several hundreds to several thousands cm^{-3}, and a shock can not penetrate these regions easily. Some fraction of Si may reside in volatile forms in dust grains which can be easily destroyed. Several forms of Si in dust grains are proposed to explain the fact that an order of 10% of Si atoms easily return to the gas phase: a volatile component with the binding energy of $E_b \simeq$ 1–2 eV (Tielens 1998), a mantle being photodesorbed by UV photons (Walmsley et al. 1999), and organometallic complexes (Klotz et al. 1995; Marty et al. 1989). The present study suggests that about 10% of Si atoms may reside in some of these forms in dust grains that are relatively easily ejected to the gas phase by UV photons. The recycling as well as the composition of dust grains in interstellar space should be reexamined based on further systematic observations of variations in different environments and other dust composing elements.

In the σ Sco region, the upper limit of the [Si II] 35 μm to [N II] 122 μm intensity ratio indicates that the Si abundance in the ionized gas should be lower than 100% of the solar abundance and no useful constraint on the abundance of Si in gas phase is obtained.

4. Summary

We observed the ρ Oph main cloud and the σ Sco region with SWS and LWS on board the *ISO*. We have detected 8 lines, [Si II] 35 μm, H$_2$ pure rotational transition lines S(0) to S(3), [O I] 63 μm, 146 μm, and [C II] 158 μm, in the ρ Oph region, and 3 fine-structure lines,

[O I] 63 μm, [N II] 122 μm, and [C II] 158 μm, in the σ Sco region.

In the ρ Oph region, the observed [O I] 146 μm emission is too strong, and the [O I] 63 μm and the [C II] 158 μm emissions are too weak compared to PDR models. As has been proposed for S171 (OOSD03), we adopt a simple model of overlapping PDR clouds along the line of sight which attenuate the [O I] 63 μm and [C II] 158 μm. We show that this model accounts for the intensities of the [O I] 63 μm, 146 μm, [C II] 158 μm, and the continuum emission at the same time. Because of the absence of the H II region in the ρ Oph, the present analysis supports the validity of the overlapping model with less ambiguity. The gas density varies over 250–2500 cm^{-3} and the surface temperature $T \sim$ 100–400 K for the ρ Oph region. In the σ Sco region, the overlapping effect is negligible and we derive physical conditions from the [O I] 63 μm emission. Comparison of the model prediction indicates that 30–80% of the [C II] 158 μm emission comes from the ionized gas in the vicinity of σ Sco.

The [Si II] 35 μm emission was observed quite strongly in the ρ Oph region. With the derived PDR properties we discuss the large Si abundance in the PDR gas in the ρ Oph region. The observed ratio of [Si II] 35 μm to the [O I] 146 μm indicates the Si abundance in the PDR gas to be 10–20% of solar, suggesting the dust destruction taking place in the PDR. This result is supported by comparison of the [Si II] 35 μm intensity with the continuum emission for $n \sim 10^3$ cm^{-3}. The present results strongly suggest that some fraction of Si atoms must be included in volatile forms in dust grains which are relatively easily destroyed. The present observation indicates the importance of the [Si II] 35 μm line in future observations to investigate the dust destruction and the composition of dust grains.

REFERENCES

André, M. K., et al. 2003, ApJ, 591, 1000

Baart, E. E., de Jager, G., & Mountfort, P. I. 1980, A&A, 92, 156

Cardelli, J. A., Meyer, D. M., Jura, M., & Savage, B. D. 1996, ApJ, 467, 334

Carral, P., Hollenbach, D. J., Lord, S. D., Colgan, S. W. J., Haas, M. R., Rubin, R. H., & Erickson, E. F. 1994, ApJ, 423, 223

Cartledge, S. I. B., Lauroesch, J. T., Meyer, D. M., & Sofia, U. J. 2004, ApJ, 613, 1037

Cartledge, S. I. B., Meyer, D. M., Lauroesch, J. T., & Sofia, U. J. 2001, ApJ, 562, 394

Caux, E., et al. 1999, A&A, 347, L1

Clegg, P. E., et al. 1996, A&A, 315, L38

Colgan, S. W. J., Haas, M. R., Erickson, E. F., Rubin, R. H., Simpson, J. P., & Russell R. W. 1993, ApJ, 413, 237

de Geus, E. J., Bronfman, L., & Thaddeus, P. 1990, A&A, 231, 137

de Graauw, T., et al. 1996, A&A, 315, L49

Draine, B. T. & Lee, H. M. 1984, ApJ, 285, 89

Fitzpatrick, E. L. 1996, ApJ, 473, L55

Frisch, P. C., & Slavin, J. D. 2003, ApJ, 594, 844

Fuente, A., Martín-Pintado, J., Rodríguez-Fernández, N. J., Cernichoaro, J., & Gerin, M. 2000, A&A, 1053

Gry, C., et al. 2003, The ISO Handbook, vol.III: LWS – The Long Wavelength Spectrometer, version 2.1

Haas, M. R., Hollenbach, D., & Erickson, E. F. 1991, ApJ, 374, 555

Habing, H. J. 1968, Bull. Astro. Inst. Netherlands, 19, 421

Harris, A. W., Gry, C., & Bromage, G. E. 1984, ApJ, 284, 157

Habart, E., Boulanger, F., Verstraete, L., Pineau des Forêts, G., Falgarone, E., & Abergel, A. 2003, A&A, 397, 623

Hollenbach, D. J., Takahashi, T., & Tielens, A. G. G. M. 1991, ApJ, 377, 192

Jenkins, E. B., Savage, B. D., & Spitzer, L. 1986, ApJ, 301, 355

Jensen, A. G., Rachford, B. L., & Snow, T. P. 2005, ApJ, 619, 891

Jones, A. P. 2000, JGR, 105, 10257

Jones, A. P., Tielens, A. G. G. M., Hollenbach, D. J, & McKee, C. F. 1994, ApJ, 433, 797

Jones, A. P., Tielens, A. G. G. M., & Hollenbach, D. J. 1996, ApJ, 469, 740

Kamegai, K., et al. 2003, ApJ, 589, 378

Kaufman, M. J., Wolfire, M. G, Hollenbach, D. J., & Luhman, M. L. 1999, ApJ, 527, 795

Kessler, M. F., et al. 1996, A&A, 315, L27

Klotz, A., Marty, P., Boissel, P., Serra, G., Chaudret, B., & Daudey, J. P. 1995, A&A, 304, 520

Leech, K. et al. 2003, The ISO Handbook, vol. V: SWS - The Short Wavelength Spectrometer, version 2.0.1

Liseau, R., et al. 1999, A&A, 344, 342

Loren, R. B. 1989, ApJ, 338, 902

Marty, P., Serra, G., Chaudret, B., & Ristorcelli, I. 1994, A&A, 282, 916

Mathis, J. S. 1990, ARA&A, 28, 37

Meixner, M. & Tielens, A. G. G. N. 1993, ApJ, 405, 216

Mizutani, M., Onaka, T., & Shirabi, H. 2004, A&A, 423, 579

Okada, Y., Onaka, T., Shibai, H., & Doi, Y. 2003, A&A, 412, 199 (OOSD03)

Nozawa, S., Mizuno, A., Teshima, Y., Ogawa, H., & Fukui, Y. 1991, ApJS, 77, 647

Perryman, M. A. C., Lindegren, L., Kovalevsky, J., et al. 1997, A&A, 323, L49

Rosenthal, D., Bertoldi, F., & Drapatz, S. A&A, 356, 705

Savage, B. D., & Sembach, K. R. 1996, ARA&A, 34, 279

Snow, T. P., Rachford, B. L, & Figoski, L. 2002, ApJ, 573, 662

Sofia, U. J., Cardelli, J. A., Guerin, K. P., & Meyer, D. M. 1997, ApJ, 482, L105

Sofia, U. J., Cardelli, J. A., & Savage, B. D. 1994, ApJ, 430, 650

Stolovy, S. R., Herter, T., Gull, G. E., Pirger, B., & Vogt, N. P. 1995, in ASP Conf. Vol 73, Airborne Astronomy Symposium on the Galactic Ecosystem: From Gas to Stars to Dust, ed. Haas, M. R., Davidson, J. A., & Erickson, E. F., p.469

Tielens, A. G. G. M. 1998, ApJ, 499, 267

Tomono, D., Onaka, T., Yui, Y. Y., Nakagawa, T., & Shibai, H. 1997, ASP Conference Series, 124, 278

Walmsley, C. M., Pineau des Forêts, G., & Flower, D. R. 1999, A&A, 342, 542

Wolfire, M. G., Tielens, A. G. G. M., & Hollenbach, D. 1990, ApJ, 358, 116

Young Owl, R. C., Meixner, M. M., Fong, D., Haas, M. R., Rudolph, A. L., & Tielens, A. G. G. M. 2002, ApJ, 578, 885

Yui, Y. Y., Nakagawa, T., Doi, Y., Okuda, H., Shibai, H., Nishimura, T., & Low, F. J. 1993, ApJ, 419, L37

Table 1. Summary of the forbidden-line intensities in the ρ Oph region

No.	R.A.[a]		DEC.[b]	d^{c}	line intensities ($10^{-8}\,\mathrm{W\,m^{-2}\,sr^{-1}}$)			
	m	s	s	pc	[Si II] $35\,\mu$m	[O I] $63\,\mu$m	[O I] $146\,\mu$m	[C II] $158\,\mu$m
1	22	37.15	39.83	1.50	< 2.73	< 2.15	< 0.34	4.12 ± 0.17
2	22	50.33	41.17	1.39	< 2.72	< 3.07	< 0.42	3.54 ± 0.17
3	23	3.52	42.45	1.27	< 2.82	< 2.73	< 0.36	3.26 ± 0.21
4	23	16.70	43.66	1.15	< 2.40	< 2.81	< 0.31	4.50 ± 0.22
5	23	29.88	44.80	1.03	< 3.10	< 3.24	< 0.39	5.15 ± 0.59
6	23	43.07	45.86	0.91	< 1.77	< 2.29	< 0.39	5.42 ± 0.20
7	23	56.24	46.85	0.79	< 2.53	< 2.24	< 0.34	6.07 ± 0.32
8	24	9.43	47.77	0.67	< 2.47	< 2.93	< 0.51	6.11 ± 0.22
9	24	22.60	48.62	0.56	< 2.87	< 2.96	< 0.27	6.80 ± 0.27
10	24	35.79	49.41	0.44	< 2.54	< 2.86	< 0.53	8.02 ± 0.31
11	24	48.97	50.11	0.32	< 2.28	< 2.97	< 0.59	9.30 ± 0.48
12	25	2.15	50.75	0.20	< 2.63	< 2.63	< 0.34	10.66 ± 0.64
13	25	15.34	51.31	0.08	3.61 ± 0.97	< 4.29	0.73 ± 0.11	11.43 ± 0.63
14	25	28.52	51.80	0.04	5.90 ± 1.06	4.05 ± 1.25	1.23 ± 0.25	17.85 ± 1.63
15	25	41.70	52.22	0.16	7.26 ± 1.07	10.05 ± 1.41	3.25 ± 0.81	21.17 ± 1.12
16	25	54.88	52.57	0.28	5.12 ± 0.91	12.32 ± 1.31	1.78 ± 0.32	22.21 ± 1.19
17	26	8.06	52.85	0.39	3.28 ± 0.84	10.57 ± 1.11	2.12 ± 0.36	20.55 ± 1.13
18	26	21.25	53.06	0.51	< 3.36	6.92 ± 1.14	2.37 ± 0.16	17.97 ± 0.90
19	26	34.43	53.20	0.63	< 2.15	3.29 ± 0.92	0.98 ± 0.22	10.21 ± 0.56
20	26	47.62	53.26	0.75	< 2.87	2.64 ± 0.81	0.69 ± 0.19	8.18 ± 0.42
21	27	0.79	53.25	0.87	< 3.69	< 2.48	< 0.55	7.05 ± 0.40
22	27	13.98	53.17	0.99	< 2.25	< 3.54	< 0.55	6.31 ± 0.32
23	27	27.16	53.03	1.10	< 3.38	2.94 ± 0.82	< 0.79	5.77 ± 0.42
24	27	40.34	52.80	1.22	< 2.29	< 2.30	< 0.34	4.72 ± 0.30
25	27	53.53	52.51	1.34	< 3.60	< 2.84	< 0.48	4.08 ± 0.18
26	28	6.71	52.14	1.46	< 2.14	< 2.51	< 0.47	3.74 ± 0.17
27	28	19.89	51.71	1.58	< 2.63	< 2.52	< 0.43	2.74 ± 0.16
28	28	33.07	51.20	1.70	< 2.96	< 2.21	< 0.36	2.48 ± 0.20
29	28	46.25	50.62	1.82	< 2.65	< 2.41	< 0.29	2.38 ± 0.28
30	28	59.44	49.97	1.94	< 3.05	< 2.52	< 0.38	2.81 ± 0.19

Table 1—Continued

No.	R.A.[a]		DEC.[b]	d[c]	line intensities ($10^{-8}\,\mathrm{W\,m^{-2}\,sr^{-1}}$)			
	m	s	s	pc	[Si II] 35 μm	[O I] 63 μm	[O I] 146 μm	[C II] 158 μm
31	29	12.62	49.25	2.05	< 2.34	< 2.68	< 0.26	2.51 ± 0.16
32	29	25.81	48.45	2.17	< 2.04	< 2.22	< 0.27	2.31 ± 0.15

[a]16h (J2000)

[b]−24°27′ (J2000)

[c]Distance from HD 147889

Table 2.   Summary of the H$_2$ line intensities in the ρ Oph region.

position	line intensities (10^{-8} W m^{-2} sr^{-1})[b]							
	v=1-0 O(3) 2.80 μm 14″ × 20″	v=2-1 O(3) 2.97 μm 14″ × 20″	v=1-0 O(5) 3.23 μm 14″ × 20″	v=2-1 O(9) 4.91 μm 14″ × 20″	v=0-0 S(3) 9.66 μm[a] 14″ × 20″	v=0-0 S(2) 12.3 μm 14″ × 27″	v=0-0 S(1) 17.0 μm 14″ × 27″	v=0-0 S(0) 28.2 μm 20″ × 27″
13	–	–	–	–	< 2.01	–	–	< 3.44
14	–	< 1.67	< 1.43	< 8.76	< 3.00	< 23.71	3.80±0.96	< 5.73
15	–	< 1.30	< 1.44	< 6.71	3.49±0.61	< 19.88	8.96±1.00	< 3.58
16	–	< 3.46	< 2.42	< 11.49	2.79±0.72	< 15.78	5.53±0.79	< 3.50
17	–	< 3.28	< 2.55	< 9.16	5.72±0.65	< 23.82	12.21±1.10	< 4.10
18	< 3.31	< 2.34	< 2.50	< 15.75	8.41±0.83	17.17±3.14	18.15±1.22	4.03±1.25
19	–	–	< 0.77	< 5.33	< 1.98	–	2.52±0.77	< 3.09
20	–	–	–	–	< 1.89	–	–	< 2.75

[a]The upper limit of the 9.66 μm intensities at the observed positions not listed here are 3.0×10^{-8} W m^{-2} sr^{-1}.

[b]The third row indicates the aperture size of the SWS. Lines with – indicate that the observation was not been carried out.

Table 3. Summary of the line intensities in the σ Sco region.

No.	R.A.[a]		DEC.[b]		d^{c}	line intensities ($10^{-8}\,\mathrm{W\,m^{-2}\,sr^{-1}}$)		
	m	s	m	s	pc	[O I] $63\,\mu$m	[N II] $122\,\mu$m	[C II] $158\,\mu$m
1	19	13.73	9	5.90	1.55	1.14 ± 0.36	< 0.23	2.14 ± 0.21
2	19	23.10	11	13.20	1.43	0.82 ± 0.27	< 0.18	2.68 ± 0.15
3	19	32.48	13	20.50	1.30	< 1.00	< 0.21	2.82 ± 0.21
4	19	41.87	15	27.70	1.18	< 1.36	< 0.27	3.74 ± 0.16
5	19	51.26	17	34.90	1.05	1.73 ± 0.29	< 0.42	4.37 ± 0.20
6	20	0.65	19	42.10	0.93	1.67 ± 0.36	< 0.28	4.45 ± 0.18
7	20	10.05	21	49.30	0.81	1.14 ± 0.36	0.34 ± 0.09	4.71 ± 0.23
8	20	19.46	23	56.40	0.68	< 1.23	< 0.59	4.53 ± 0.19
9	20	28.87	26	3.40	0.56	< 1.07	0.44 ± 0.14	4.23 ± 0.22
10	20	38.29	28	10.50	0.43	< 1.32	0.40 ± 0.11	4.44 ± 0.19
11	20	47.71	30	17.40	0.31	< 1.04	< 0.27	3.47 ± 0.13
12	20	57.14	32	24.40	0.19	< 1.44	< 0.25	3.29 ± 0.17
13	21	6.58	34	31.30	0.06	< 1.47	0.34 ± 0.08	2.46 ± 0.17
14	21	16.02	36	38.20	0.06	< 1.22	< 0.29	2.57 ± 0.10
15	21	25.46	38	45.00	0.19	< 1.06	< 0.30	2.65 ± 0.10

[a]16h (J2000)

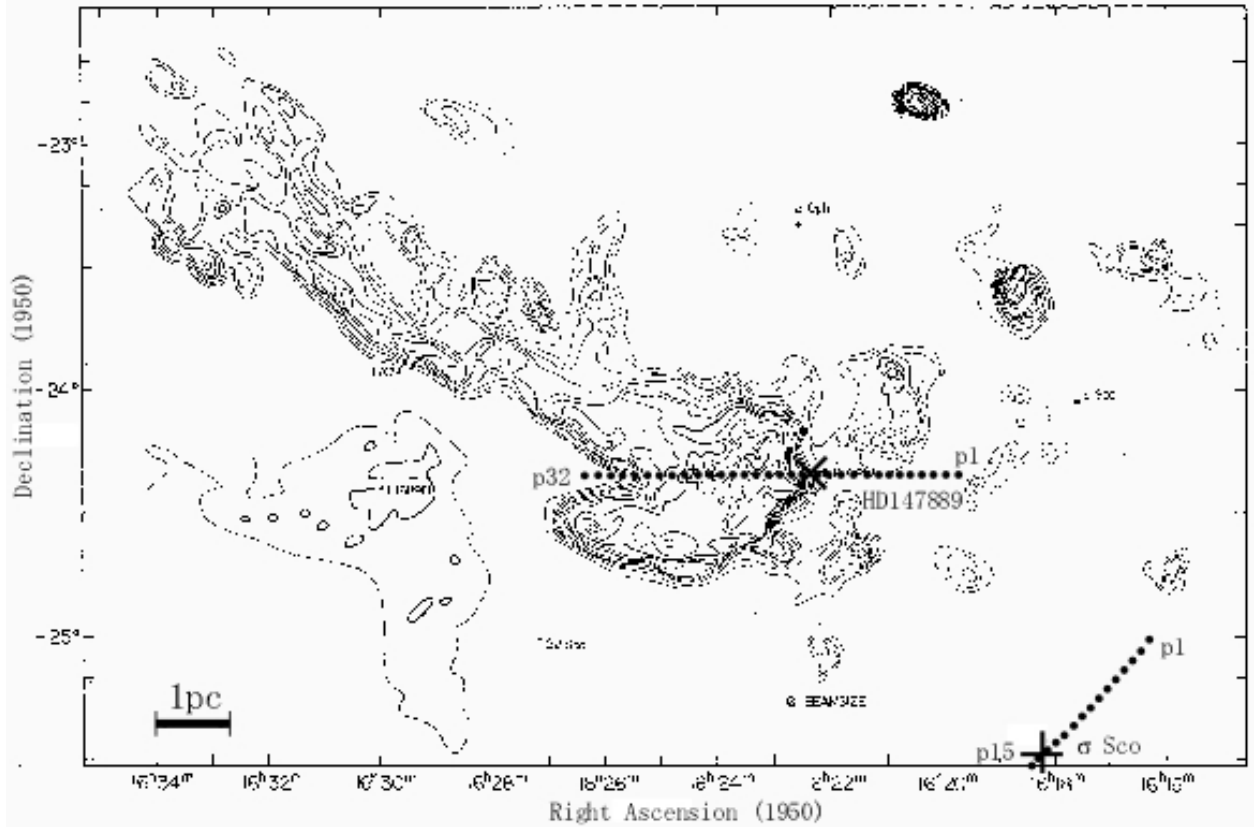[b]$-25°$ (J2000)

[c]Distance from σ Sco

Fig. 1.— Observed positions of the ρ Oph and σ Sco region. The ^{13}CO ($J = 1$–0) peak temperature is shown in contours (Loren 1989). The positions of HD 147889 and σ Sco star are shown by crosses. The black circles show the observed positions and the size of the circles indicates the beam size of the LWS.
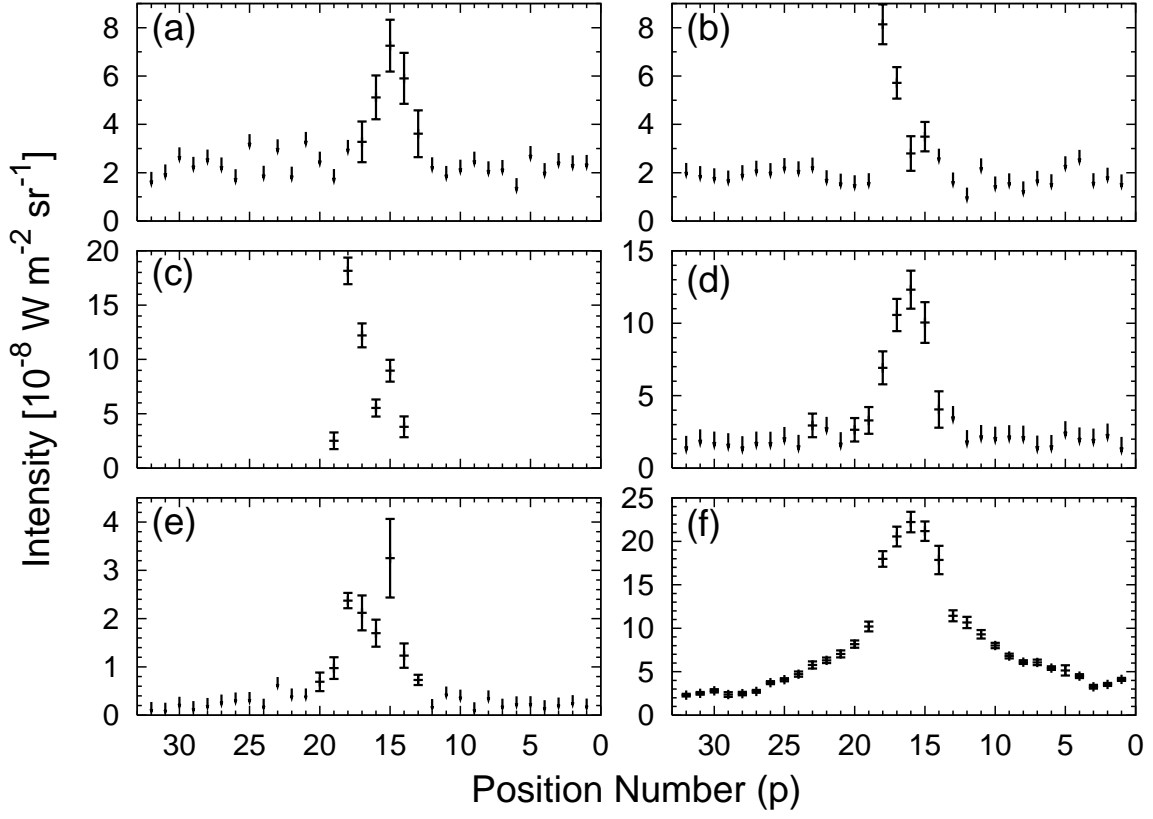
Fig. 2.— Observed line intensities in the ρ Oph region. HD 147889 is located between p13 and p14. The arrows indicate 3σ upper limits. **a)** [Si II] $35\,\mu$m; **b)** H$_2$ $9.66\,\mu$m; **c)** H$_2$ $17.0\,\mu$m; **d)** [O I] $63\,\mu$m; **e)** [O I] $146\,\mu$m; and **f)** [C II] $158\,\mu$m.
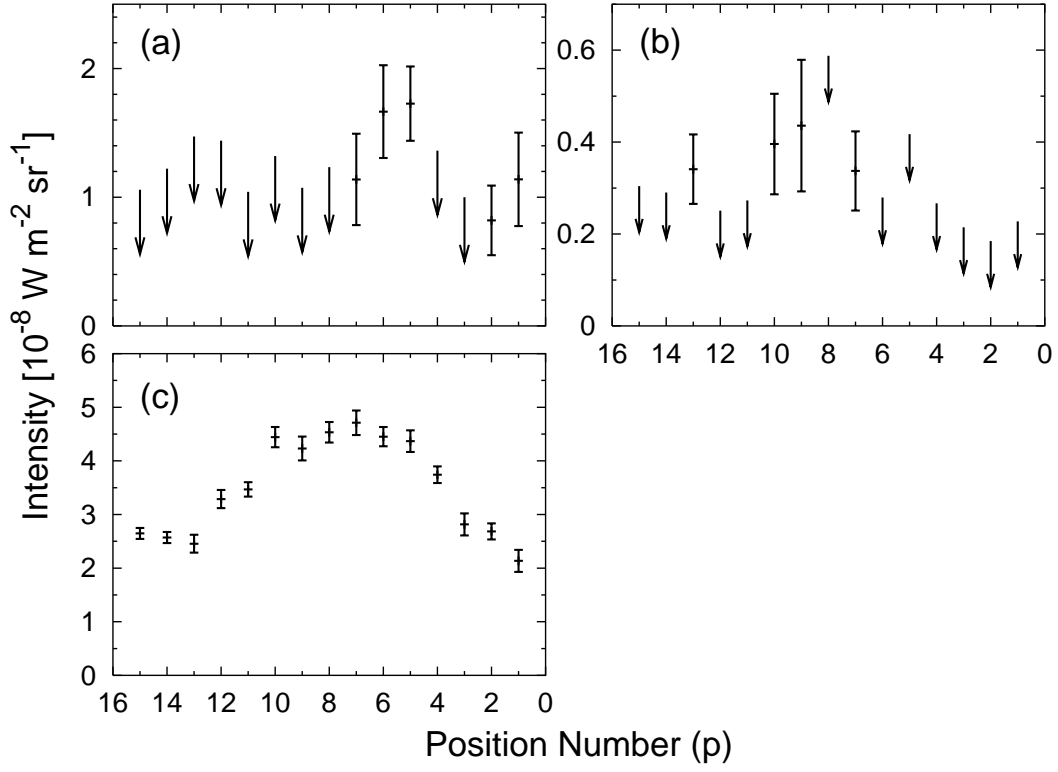
Fig. 3.— Observed line intensities in the σ Sco region. σ Sco is located between p13 and p14. The arrows indicate 3σ upper limits. **a)** [O I] 63 μm; **b)** [N II] 122 μm; and **c)** [C II] 158 μm.
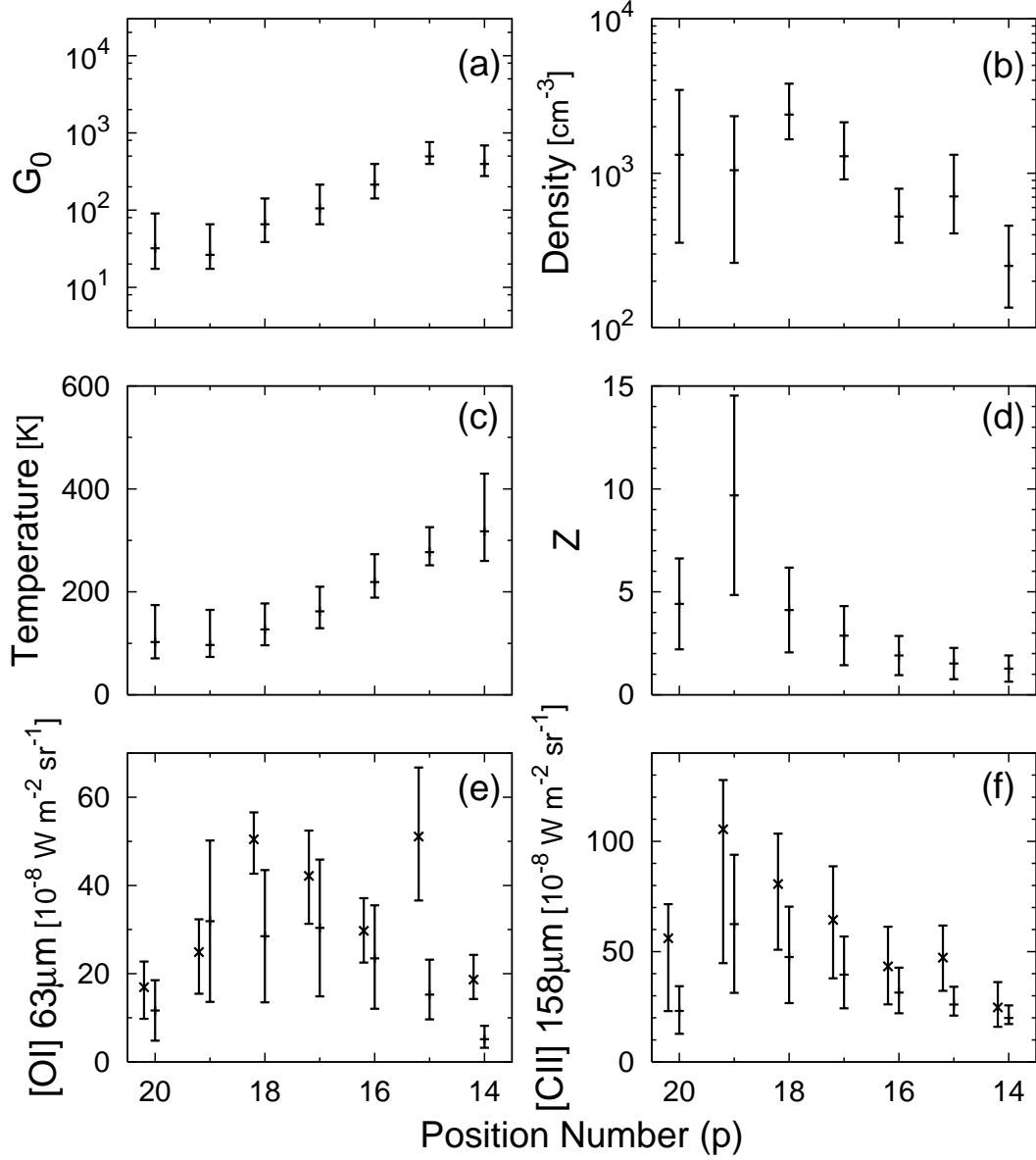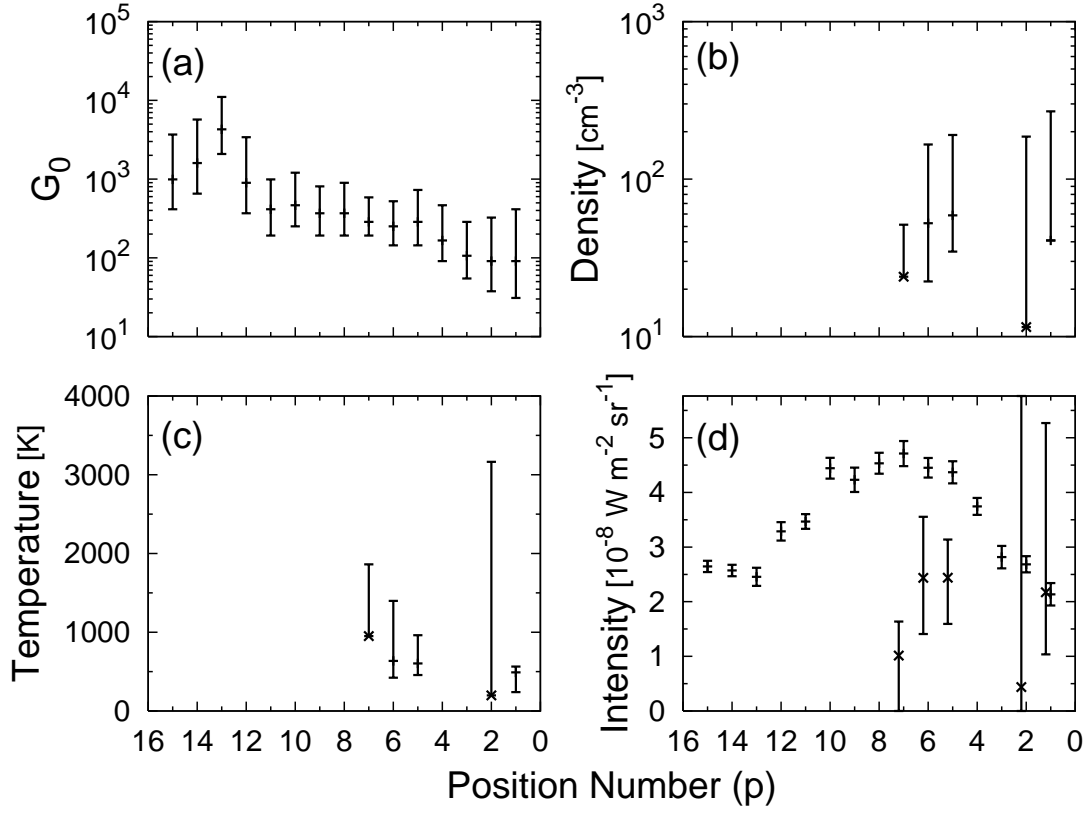
Fig. 4.— PDR properties for the ρ Oph region. **a)** Radiation field strength G_0 estimated from the continuum of the LWS spectrum (see text), **b)** gas density, **c)** surface temperature from the PDR model, **d)** overlapping factor Z (see text), **e)** model prediction of the [O I] 63 μm intensity derived from the PDR model (crosses shifted slightly to left for clarity) and the observed intensity of [O I] 63 μm after correcting the overlapping effect using Z (pluses) (see text), and **f)** same as e) but for [C II] 158 μm.

Fig. 5.— PDR properties for the σ Sco region. **a)** Radiation field strength G_0 estimated from the continuum of the LWS spectrum (see text), **b)** gas density, **c)** surface temperature, and **d)** the model prediction of the [C II] 158 μm intensity derived from the PDR model (crosses shifted slightly to left for clarity). Pluses indicate the observed [C II] 158 μm intensitiy.
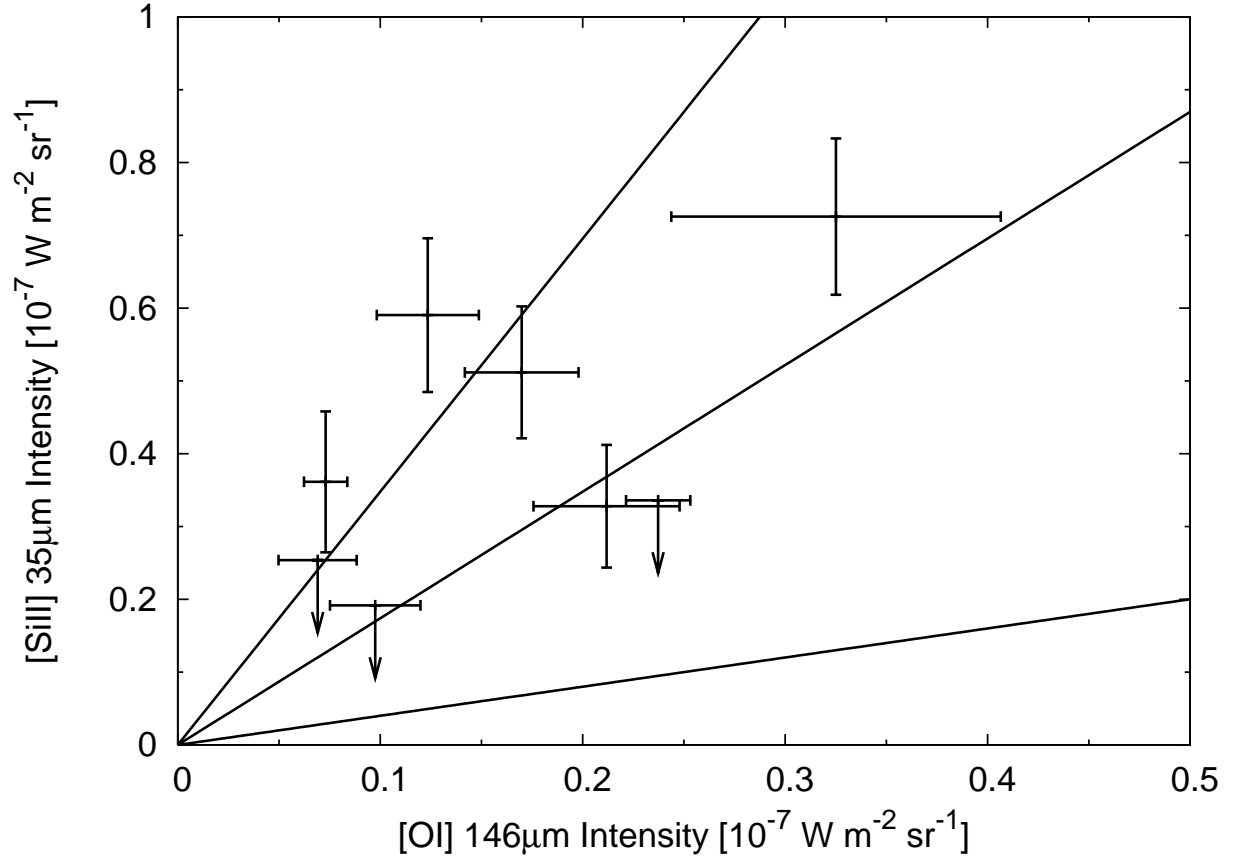
Fig. 6.— The observed [O I] 146 μm against [Si II] 35 μm line intensities at positions where at least one of them is detected. The solid lines show the Si abundance of 2.3% (PDR model), 10%, and 20% of solar from bottom to top.
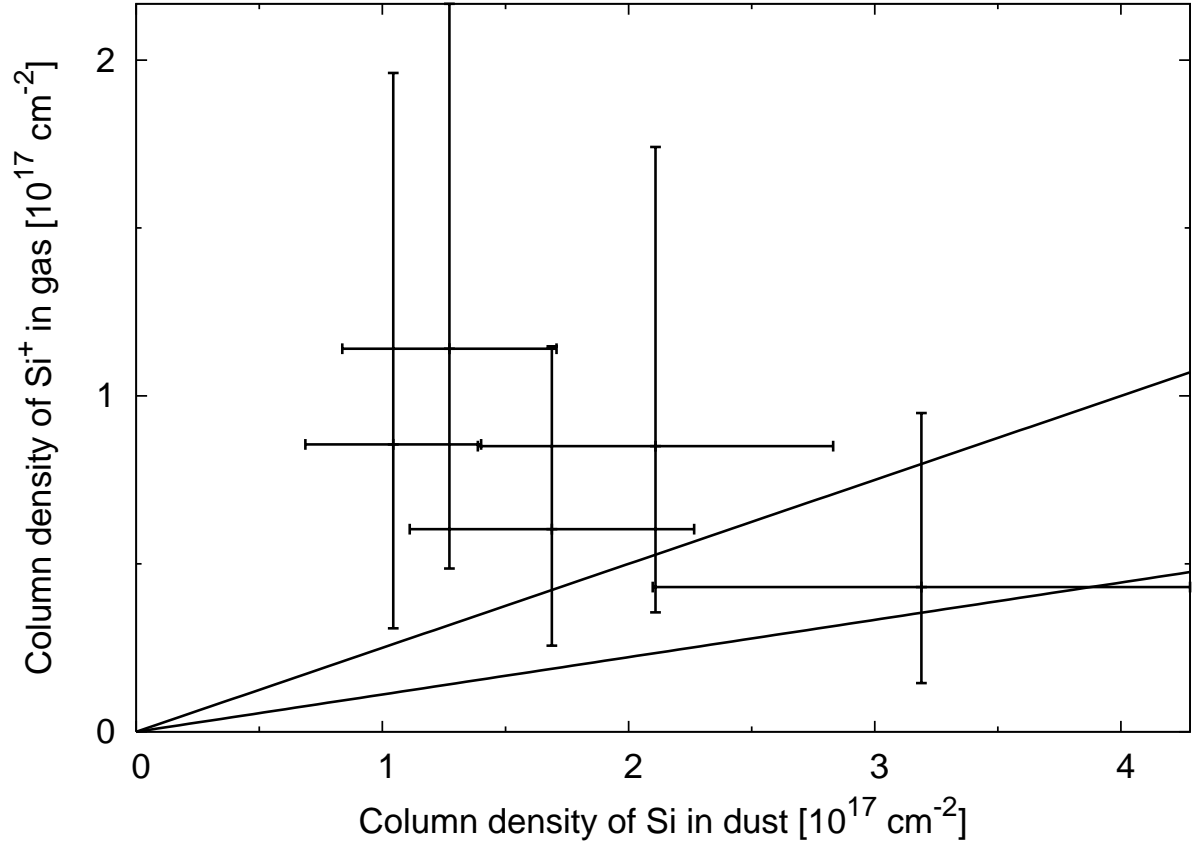
Fig. 7.— Column density of Si in dust against that in gas. Only the data at p13-p17 are plotted, where the [Si II] 35 μm emission is detected. Solid lines show the relative abundance of Si in gas : dust = 1:9 (10% is in gas phase) and 1:4 (20% is in the gas phase) from bottom to top.